High-throughput snalysis of synaptic activity in electrically stimulated neuronal cultures

High-throughput analysis of synaptic activity in electrically stimulated neuronal cultures

Michiel Van Dyck[1,2], Rajiv K. Mishra[2†], Francisco Pestana[2], Peter Verstraelen[1], Hilde Lavreysen[2], Juan D. Pita-Almenar[2], Nachiket D. Kashikar[2‡], Winnok H. De Vos[1*]

[1] University of Antwerp, Laboratory of Cell Biology and Histology, CDE, Antwerp, Belgium

[2] Janssen Pharmaceutica, Neuroscience Division, Beerse, Belgium

[†] Present address: iOligos Technologies Private Limited, 1703, CB2, Supertech Capetown, Sector-74, Noida, India 201301

[‡] Present address: Resolve BioSciences GmbH, Creative Campus Monheim Gebäude A03, Alfred-Nobel-Strasse 10, 40789, Monheim am Rhein, Germany

* Correspondence: nachiket.kashikar@resolve-biosciences.com and Winnok.DeVos@uantwerpen.be

Abstract

Synaptic dysfunction is a hallmark of various neurodegenerative and neurodevelopmental disorders. To interrogate synapse function in a systematic manner, we have established an automated high-throughput imaging pipeline based on fluorescence microscopy acquisition and image analysis of electrically stimulated synaptic transmission in neuronal cultures. Identification and measurement of synaptic signal fluctuations is achieved by means of an image analysis algorithm based on singular value decomposition. By exploiting the synchronicity of the evoked responses, the algorithm allows disentangling distinct temporally correlated patterns of firing synapse populations or cell types that are present in the same recording. We demonstrate the performance of the analysis with a pilot compound screen and show that the multiparametric readout allows classifying treatments by their spatiotemporal fingerprint. The image analysis and visualization software has been made publicly available on Github

(https://www.github.com/S3Toolbox). The streamlined automation of multi-well image acquisition, electrical stimulation, analysis, and meta-data warehousing facilitates large-scale synapse-oriented screens and, in doing so, it will accelerate the drug discovery process.

Keywords: electric stimulation, synapse, segmentation, singular value decomposition, compound screening, neurodegeneration

Introduction

Neurodegeneration is defined by the loss of neuronal connections in vulnerable brain regions resulting in memory faltering and cognitive decline. The impaired connectivity precedes the actual loss of neurons and resides in dysfunction and deterioration of synapses. Disturbances in synapse integrity are clearly detectable at early stages of Alzheimer's disease, including in patients with mild cognitive impairment (Lu et al. 2013; Tampellini 2015). They are also found in several neurodevelopmental disorders such as epilepsy and autism (Chu et al. 2010; Zoghbi and Bear 2012). Importantly, unlike neuronal loss, defects in synaptic function may be reversible. Owing to their plasticity, the function of synapses can be enhanced, their formation can be promoted, or their pruning inhibited. This makes the synapse an interesting therapeutic target. But when aiming at their modulation, methods are required to interrogate synapses with high sensitivity. In recent years several methods have been established to quantify synapse density in fixed samples (Nieland et al. 2014; Verschuuren et al. 2019; Verstraelen et al. 2020). However, these methods have limited sensitivity and do not report on the actual function of synapses. Technological advances in genetically encoded sensors and imaging methodologies have made it possible to record and manipulate the activity of neural circuits with high spatiotemporal precision (Lin and Schnitzer 2016). Now that it is possible to image dynamic signals across hundreds of neurons and synapses simultaneously, the challenge is to adequately and systematically extract quantitative information from the acquired image data sets. Whereas high-throughput screening platforms have been conceived for the analysis of pan-cellular signals such as calcium fluxes (Wardill et al. 2013), applications at the level of the synapses are much more challenging owing to their small size, high density and fast, fluctuating dynamics. High-throughput assays for synaptic function mainly cope with these caveats by averaging out

responses over an entire well (Hempel et al. 2011; Virdee et al. 2017). This, however, does not allow charting the functional heterogeneity between or within individual synapses (*e.g.,* calcium signaling and glutamate release). Another concern with reproducible interrogation of synapse functionality is that spontaneous activity is variable and unpredictable, urging for more controlled induction using optical or electrical stimuli. Yet, scalable integration of computer-controlled stimulation with single synapse readout remains non-trivial. To address this, we have created a fully integrated hardware and software pipeline to acquire synapse activity from different fluorescent reporters in a systematic and reproducible manner in 96-well plate format. Exploiting the temporal synchronicity of electrically induced signals, we implemented an active synapse detection algorithm that offers a means to remove non-informative features (such as noise) and unmix different subpopulations (by their kinetics). Using this approach, we characterize the impact of four pharmacological reference compounds and reveal different types of synapse modulation. Large-scale compound screening with this pipeline should allow for building a library of synapse modulating compounds, which can be queried for functional impact and their mechanistic underpinnings.

Methods

Cell culture

Experimental procedures were approved by the Institutional Ethical Committee on Animal Experimentation, in accordance with European Directive 2010/63/EU and local legislation (Flemish Decree on the protection of laboratory animals dd. 17 February 2017) and the facilities are AAALAC accredited (Association for the Assessment and Accreditation of Laboratory Animal Care). Hippocampi or cortices were dissected from WT E18 Wistar rat embryos in HEPES (7 mM)-buffered Hanks' Balanced Salt Solution (HBSS), followed by trypsin digestion (0.05%; 15 min; 37°C) and mechanical dissociation by trituration through 2 glass pipette tips with decreasing diameter. After centrifugation (5 min at 200g), the cell pellet was resuspended in Minimal Essential Medium (MEM) supplemented with 10% heat-inactivated horse serum and 30 mM glucose. Cells were plated in Poly-D-Lysin-coated 96-well plates (Greiner, µClear), at 30,000 cells/well, and kept in a humidified CO_2 incubator (37°C; 5% CO_2). After 2 h, the medium was replaced with B27 (2%) supplemented phenol red-free Neurobasal medium, containing Sodium Pyruvate (1 mM), GlutaMAX (2 mM), and Pen-Strep (0.2%). Cell culture supplies were purchased from ThermoFisher. Validation of synaptic connectivity was done in these cultures using immunofluorescence for pre- and postsynaptic markers, calcium imaging and patch clamp recordings (Suppl. Fig. S1).

Transduction

Primary neuronal cultures were transduced with adeno-associated viral (AAV6) vector containing either the synapse-targeted Ca^{2+} reporter SyGCaMP6f (Dreosti et al. 2009), PSD95-GCaMP6f (Mao et al. 2008) to assay postsynaptic Ca2+ changes or iGluSnFR (Marvin et al.

2013), a single-wavelength glutamate sensor, which directly and specifically reports on excitatory neurotransmitter release. Primary neurons were transduced 2 hours after plating, on the first day in vitro (DIV0) at a multiplicity of infection of 50 given the original viral titer of 10E10 viral genome copies per ml. Media was changed once at DIV2 (*i.e.,* 48 hours post-transduction) to avoid cell death before recording on DIV21-24. The AAV6 vectors were manufactured by SIRION Biotech and were commercially obtained.

Microscopy setup, image acquisition and electrical stimulation

The setup is based on the concept described by Wardill et al. (2017). In brief, the system consists of a fully automated widefield fluorescence microscope (Olympus IX83) equipped with a 40X (NA = 0.60) dry objective; a LED light source (Omicron LED HUB, GFP-470nm, 1-50 mW), an Andor Ixon Ultra 897 EM-CCD Camera, and an in house made multi-well electronic stimulation device, with individually addressable units. The electric field stimulation is done by passing a computer controlled electric current, through a pair of platinum electrodes, which touch the well surface (Fig. 1). The stimulus hardware was manufactured by Peira BVBA (Suppl. Data 1). It consists of a custom-made 96-well plate lid, that is based on a printed circuit board (PCB) onto which the pairs of 5 mm-spaced bent platinum electrodes have been mounted. The current between the individual electrode pairs is controlled on a single-well basis, by means of a solid-state relay controller box. The relays are computer controlled by a NIDAQ-board (NI USB-6363) to generate the pulses. The timing of the stimulation is done by the same NI-board. The stimulation amperage is controlled by the current source (WPI A385). The synchronization between the computer-controlled stimulus and the microscope recording is done by a microscope trigger (Andor Precision control unit series 100).

Images of fluorescent protein-coupled functional reporters were acquired with FF01-474/27-25 nm excitation, FF495-Di03-25x36 nm Dichroic, and FF01-525/45-25 nm (Semrock) emission filters at a temporal sampling rate between 30-50 fps and pixel size of 0.40 µm. During recording, the stimulation tool, an in-house created software control program (NI LabVIEW, Suppl. Data 2), ran different stimulation sequences with variable number of stimuli and frequencies on the cell to induce action potential driven synaptic transmission. In our setup, one stimulus (= 1EP) corresponded to a 1ms pulse of 5 mA current and a 10 EP pulse was generated with the same frequency (20Hz).

Compound treatment

At the time of recording, medium was gently replaced with a recording buffer of which the composition varied depending on the compound. For most regular recordings, this buffer was normal extracellular solution (NES, 136 NaCl, 2.5 KCl, 10 HEPES, 1.3 $MgCl_2$, 10 glucose, 2 $CaCl_2$, pH 7.4), for PSD-GCaMP6f experiments, we made use of modified NES buffer containing the NMDA receptor agonist glycine, to ascertain sufficient NMDA activation (119 NaCl, 2.5 KCl, 25 HEPES, 2 $MgCl_2$, 30 glucose, 2 $CaCl_2$, pH 7.4, additionally, 50 µM Glycine) and for SyGCaMP6f experiments in which excitatory synaptic transmission was blocked to reduce spontaneous activity, NES was supplemented with 10 µM NBQX disodium salt and 50 µM DL-AP5 (NES^{++}).

The following reference compounds (Tocris) were used: the glial glutamate transporter EAAT1 and EAAT2 inhibitor threo-beta-benzyloxyaspartate (TBOA; 100nM), the potent, non-substrate EAAT2 inhibitor WAY213613 (WAY; 10µM), the selective and reversible Na^+ channel conductance inhibitor tetrodotoxine (TTX; 1µM), and protein kinase C activator phorbol 2-

myristate 13-acetate (PMA; 1µM). 0.1% dimethyl sulfoxide (DMSO) or medium with blockers only were used as control.

Image and data analysis

A dedicated software processing pipeline, called Stimulated Synapse Segmentation Tool (S^3T) (https://www.github.com/S3Toolbox), was written in Matlab (Mathworks inc.) for batch image processing, analysis, and visualization (Fig. 2; Suppl. Data 3). The software follows these steps for each unprocessed image data set: first, the raw image data (time-lapse stack) is loaded along with metadata regarding the experimentation procedure (*e.g.,* compound type and concentration per well), the image acquisition settings (*e.g.,* well number, position in the well, acquisition speed) and the electrical stimulation pattern (*e.g.,* number and timing of stimuli). After background removal by setting the 5% darkest pixels to zero and bleach correction using a double exponential fit, internal quality control parameters are generated (*e.g.,* the mean temporal response curve and the average intensity image). Next, individual synapses are detected. Given that signal fluctuations are evoked by electrical stimuli, synaptic signals can be identified as regions that display correlated temporal changes. Pixels with large intensity fluctuations over time are expected to be active synapses. Hence the simplest method that is implemented to enhance the signals is based on calculating the standard deviation of the intensity over time per pixel. This method is however susceptible to variations in baseline fluorescence and also offers no resolution of the actual underlying patterns. Therefore, we have implemented a second method to enhance synaptic signals that is based on singular value decomposition (SVD) (Fig. 4). The SVD decomposes the raw recordings into a product of components according to the formula: M = USV', with matrix M the standard factor-k flattening

of the video-data (Lathauwer et al. 2000), U the matrix with left eigenvectors, here referred to as eigenframes, V the matrix with right eigenvectors, referred to as eigenresponses and S the diagonal matrix with singular values ranked by size (Eckart and Young 1936; Lathauwer et al. 2000). The rank of the eigenvectors determines their relative contribution to the variance of the image stack with the first eigenvectors encoding the most dominant spatiotemporal information. The first 16 SVD components are stored to enable fast, compressed, noise-reduced reconstruction of the recordings (Eckart and Young 1936). After the decomposition, one (typically the second, cfr. down) eigenframe is selected for synapse detection. The software also offers a method to introduce a user-defined library, thus extending the SVD algorithm to a tailored version in which the user supplies a dictionary of predefined responses (DICT, as matrix V). This is useful when the expected response is known, and the decomposition has to be consistent across multiple experiments. After synapse enhancement, there is a possibility to apply further spatial filtering or to immediately proceed to the actual segmentation, which is achieved by means of an automatic (Otsu 1979) thresholding algorithm. After hole-filling and single-pixel removal, each synapse is uniquely identified and saved as region of interest (ROI). Once detected, synapse activity is measured. Before extraction of intensity fluctuations, the images are background corrected by subtracting the average signal intensity of the 5% darkest pixels in the movie. Then, the raw traces are extracted per synapse and each trace is normalized to the initial intensity ($\Delta f / f_0$) to compensate for signal marker heterogeneity. Based on the stimulation timing parameters, the response to each electrical stimulation is extracted and analyzed. Such response typically takes the form of a fast impulse, followed by a variable decay. From the temporal traces, a set of descriptors is extracted for each synapse (Suppl. Data 4). These descriptors are averaged across the entire image to yield 20 summary statistics per field

of view in a well. In addition, spatiotemporal statistics of the unprocessed images are calculated as well. Next to these quantitative metrics, the raw and the $\Delta f/f_0$ traces are saved for each synapse as well as 4 summary traces, *i.e.,* a pixel average $\Delta f/f_0$, synapse average $\Delta f/f_0$, synapse size-weighted average ($\sum$ (synapseSize x $\Delta f/f_0$) / ($\sum$ synapseSize)), and a raw pixel average. A data viewer is embedded in the software to navigate through the different levels of the results, from the individual synapse over the well and plate level up to the experiment and compound level.

Because of the large volume of microscope data and the fast speed with which the data is (continuously) generated (15Gb/plate in < 1 hour), multiple design considerations were made to cope with this challenge. 1) The algorithms make use of the multi-core optimized SVD in Matlab to accelerate the image segmentation. 2) Multiple wells are processed in parallel to speed up the processing. This results into a processing time of ~1 hour for 1 plate (60 well-recordings of 16 s = 500 frames of 512x512 pixels at 16 bit = 15 Gb data), using 1 x 48 core machine. The processing speed was further increased by automatically distributing the work on multiple computers in a compute cluster. From a user point of view, the user interface is developed to process multiple batches of recordings, with minimal user interaction. Visualization, curation, and filtering of the extracted synapse data is all done in the same software, allowing to link together the datasets at the different stages of processing: *e.g.,* in the previously shown plots, each data point can be linked back to the original synapse recording.

Results

High-throughput imaging allows assessment of synapse activity at multiple scales

We have conceived a pipeline for measuring synaptic activity in neuronal cultures in multi-well plate format. When considering fast temporal behavior like synaptic activity, a tradeoff must be made between acquisition speed, resolution and contrast (SNR). Therefore, we first determined the applicability of the pipeline to different genetic reporters in primary hippocampal neurons from rat, namely iGluSnFR (to report glutamate release from individual synaptic terminals), cytosolic GCaMPf (neuronal calcium levels), SyGCaMP6f (presynaptic calcium levels) and PSD95-GCaMP6f (post-synaptic calcium levels). First, we tested whether electrical pulses evoked a response in iGluSnFR upon single or multiple stimulation. We found that the electric stimuli caused a measurable increase in the fluorescence intensity (Fig. 3a). The average intensity of the response across the field of view scaled with the stimulus as exemplified by the larger amplitude for 10 EP vs. 1EP (n = 60 wells) (Fig. 3b,c). The response followed the stimulation pattern even when applying narrow time intervals between consecutive stimuli, although fast stimulation seemed to be associated with short-term depression, plausibly because of decreasing availability of synaptic vesicles (Fig. 3d). When extending the approach to other markers, it became evident that their expression level (average intensity) and location pattern differed substantially (Fig. 3e). The dynamic response to 1EP and 10EP stimulation showed similar kinetics as for iGluSnFR albeit with different base level and amplitude (Fig. 3f).

While the time-lapse acquisitions had sufficient dynamic range to reliably capture the signal fluctuations, the SNR of individual time frames was too low to enable accurate delineation of structural features such as synapses. Taking advantage of the repetitive nature of the image

content, we found that the contrast could be significantly improved by using different projection methods (Fig. 3g). Using super-resolution radial fluctuations (SRRF) (Gustafsson et al., 2016) we could reconstruct images with a resolution below the diffraction limit of the microscope, offering superior detection of sub-cellular details including dendritic spines in PSD95-GCaMP6f transduced cells (Fig. 3g,h; Suppl. Movie 1). Since SRRF resolution scales with the temporal activity in the image set at hand, electrical stimulation patterns can be optimized to maximize the temporal dynamics and so boost the resolving power of SRRF per frame. Thus, the acquired images provide functional as well as morphological readout.

When aiming for high-resolution, high-speed acquisitions, the field of view (FOV) will always be limited due to optical and computational constraints. The electrical stimulation paradigm offers an elegant means to bypass this limitation, as it allows sequential stimulation and recording of different fields in a single well at fixed intervals, which can subsequently be stitched and synchronized so as to represent a *pseudo-real-time* recording of a large cell population or full well (Fig. 3h; Suppl. Movie 2). Thus, the platform offers the possibility to acquire information about synaptic activity at scales ranging from ~ 100 nm to > 1 cm, from single synapse morphology to intra-neuron network dynamics.

SVD is a robust approach for synapse analysis

After having explored the acquisition parameters and scalability of the platform, we next tested the performance of the synapse detection algorithm. To this end, we first analyzed the eigenspace, as created by SVD. We found that the majority of the variance (70-95%) was explained by the first two eigenvectors (Fig. 4a). When scrutinizing the individual eigenvectors, we found that the first eigenresponse was dominated by the base fluorescence with a slowly

decaying bleach component, whereas the second eigenresponse most prominently encoded the stimulus response (Fig. 4b). More precisely, the second eigenframe encoded the difference between the responding and non-responding structures in electrically stimulated cultures for different markers (Fig. 4b). Higher-order eigenvectors usually displayed much more variability between individual wells and progressively contained more noise components. Hence, we selected this eigenframe for the detection of synapses. To evaluate the segmentation performance on this image, we compared it with that of a standard method on simulated data. Assuming that synapses will be the regions that respond with largest speed and dynamic range to the electrical stimuli, the simplest approach to facilitate their detection is to project the stacks according to the standard deviation (STD) through time. This approach reduces noise and selectively enhances time-variant objects. However, since the standard deviation does not discriminate correlated from uncorrelated activity, this approach may also lead to the detection of spurious signals. This became clear when running the algorithm on simulated recordings of neurons undergoing 2 consecutive 1EP stimulations or a 10EP stimulation (Fig. 4c). The simulation included soma, responding and non-responding synapses, photobleaching, and a background intensity gradient and was run for 6 different SNR levels. While both STD and SVD perform well (*i.e.,* detect all simulated active synapses) under low noise levels, the STD approach rapidly succumbs under conditions of higher noise levels, whereby it starts to include non-responding synapses and soma regions (Fig. 4c). Repeating the simulation 60 times with different photobleaching and noise levels revealed a significantly lower amount of segmentation errors for SVD over STD as defined by the lower number of misclassified pixels (Fig. 4d). When specifying the expected responses using a dictionary (DICT), the SVD approach could be improved to also identify signals at the highest noise levels. However, the dictionary

approach can only be used when the synapse response pattern is known in advance. Yet, SVD offers a flexible means to extracting synaptic signals.

SVD allows spatiotemporal unmixing of synapses and cell types

Decomposing an iGluSnFR recording into its constituent eigenframes offers a means to reveal the complete spatiotemporal dynamics in a single field of view. Indeed, when combining color-coded versions of individual eigenframes, correlated and uncorrelated intensity fluctuations became visible as well as the difference in dynamics of synaptic vs. somatic responses (Fig. 5; Fig. 6a). When applying this same principle to recording of SyGCaMP6f and cytosolic GCaMP6f transduced cultures, synchronously firing neurons could easily be discriminated from non-responsive neurons (Fig. 6a,b). The color-coding principle could easily be extended to the full time-lapse acquisition, by including the eigenresponses. When applied to a PSD95-GCaMP6f movie, we could for example distinguish the background fluorescence (bleaching) (E1), the synapse activity (E2) and uncorrelated cellular activity (E3-16) at once (Fig. 6c). Because of this superior capability of SVD at detecting temporally correlated signals in an unsupervised manner, we hypothesized that it could also be used for separating cell-type specific kinetics, as often observed in co-cultures when using pan-cellular calcium sensors. Hence, we tested it on a recording of neuronal cultures, loaded with the non-cell-selective calcium dye Fluo-4AM. We found that neuronal and astrocyte calcium fluctuations could be easily distinguished based on their relative contribution to the SVD components. The glutamate pulse that solely induces neuronal response led to a prominent signal in the 2nd eigenvector (E2) whereas the astrocyte signals were more prominent in higher eigenvectors (E3-16) (Fig. 6d, Suppl. Movie 3).

Dictionary for consistent feature extraction

Using SVD, we were able to accurately detect and measure synapse activity in evoked cultures. Applied to recordings of iGluSNFR-transduced and PSD95-GCaMP6-transduced neurons, we also revealed the probabilistic nature of synaptic transmission, emphasizing its added value (Suppl. Fig. S2). By default, eigenframe 2 was used for synapse segmentation. However, unexpected cellular behavior such as spontaneous cell activity, large changes in cellular responsiveness or cell death can contribute significantly to the temporal kinetics and may therefore change the typical ordering of the eigenvectors. Also, in the absence of evoked synapse activity, the 2nd eigenvector does not encode a synapse response, but rather represents spontaneous activity or noise. That is why we have built in a manual curation possibility to switch the source eigenframe. Yet, when aiming for high-throughput screening (HTS) of multiple plates per day, manual interventions should be minimized. Hence, we adapted the SVD approach to cater for different possible scenarios, by specifying a predefined eigenresponse set in a dictionary (DICT). The dictionary can be manually created, or it can be an SVD of a quality-assed real or simulated reference recording. Its use allows systematic comparison of recordings with variable background or severe pharmacological effects and is computationally 10-100x faster than SVD calculation.

Integrated synapse activity analysis enables classification of compound effects

To evaluate the performance of our analysis, we ran a small-scale compound assay, in which we subjected primary cortical neurons, transduced with iGluSnFR to a stimulation scheme of 1 EP and 10 EP, separated by 8 seconds. The following compounds were used: WAY-213,613 (WAY), Tetrodotoxine (TTX), threo-beta-Benzyloxyaspartate (TBOA), Phorbol 2-myristate

13-acetate (PMA). Blockers only (vehicle) and DMSO served as controls. Each compound treatment was replicated 9 times, randomly distributed over the different wells of the plate. When analyzing the temporal response of synaptic regions, we found marked differences between treatments (Fig. 7a). In brief, TTX virtually abolished the response to the electrical stimulus, whereas PMA had the opposite effect and significantly increased the amplitude (+ 200%). WAY, in turn, prolonged the decay time as compared to the controls (+70%). TBOA decreased the amplitude (-75%) and prolonged the decay time (+35%) (Fig. 7b). When comparing the well-averaged synapse response to the average signal fluctuations calculated across the entire FOV, we found that the dynamic range was (+40%) higher, proving higher sensitivity for this approach (Fig. 7b). Only considering amplitude and decay time was not sufficient to irrefutably discriminate compound treatments (Fig. 7c). Hence, we explored the feature space in more detail. To do so, we compared the distribution of each parameter for a given condition with that of the control group, using a separation score, defined by the inverse of the overlap between two conditions:

$$\text{separation score (A,B)} = 1 - simScore(A,B),\ simScore(A,B) = \frac{2\ area(A \cap B)}{area(A) + area(B)}$$

This revealed how the different parameters are affected by a treatment. For instance, WAY had a large influence on the Area Under the Curve (AUC) and base fluorescence and no influence on the synapse size (Fig. 7d) compared to the cells only treated with blockers.

Given these unique effects, we reasoned that an integrative approach would allow separating treatments better, which could be of use for predicting mode of action. We used linear discriminant analysis (LDA) on all extracted parameters to define best separating hyperplane between two conditions. The coefficients defining this plane represent the relative contribution of the parameters that differentiate two treatments. In the case of PMA, we found that amplitude

was the major contributor to the LDA hyperplane, as also revealed by a scatterplot (Fig. 7e). The separation score based on the histogram of a projection onto the dominant LDA plane provided a quantitative view on the difference between two compound treatments. When compiling the separations scores for all compound combinations, the resulting compound similarity matrix (Fig.7f), showed that different treatments can be differentiated (low similarity scores) and that typical controls (blockers and DMSO) have a high similarity score. This suggested that the similarity matrix can be used to identify compounds with (dis)similar mode of action. More specific similarity measures could be obtained by limiting the matrix calculation to a subset of the features. For example, when selecting only amplitude-related features (ampss_1, synapseAmplitude1), we found that WAY-treated neurons behave quite similar as the control-treated. Similarly, when investigating the decay time matrix (downHalfTime1, tau_1), PMA resembled DMSO and blockers indicative of its limited impact on this aspect of the kinetics. In other words, integrated synapse activity analysis offers a flexible means to identify compound mode of action.

Discussion

We have created a fully integrated pipeline to interrogate synapse activity. Synapse activity can entail calcium, pH or glutamate oscillations, and, owing to the high information content, efficient SRRF-based super-resolution reconstruction facilitates morphological analyses of the same images. Furthermore, by stitching sequentially recorded time stacks of electrically stimulated recordings, the effective FOV can be significantly increased, allowing for uncovering spatial subdomains of correlated activity. While the latter should obviously first be validated using whole well recordings, it does show the robustness of the system and reproducibility of the evoked responses. Thus, the platform offers the possibility to acquire information about synaptic activity at scales ranging from ~ 100 nm to > 1 cm, from single synapse morphology to population dynamics.

At the heart of the image analysis, is a decomposition of temporally correlated information by means of SVD. We found that SVD outperforms more classical approaches for synapse detection such as STD. But we also show that at a larger scale it offers a means to untangle complex relationships and subpopulations in the image, such as differentially firing neurons and astrocytes. This offers functionality similar to recent label-free cell segmentation and *in-silico* labeling methods (Christiansen et al. 2018; Johnson et al. 2017; Pnevmatikakis et al. 2016), but with a directly traceable mathematical basis. We tailored it here for stimulated high-throughput synapse recordings but with even larger FOV recordings, SVD can also be used to investigate network dynamics in neuronal cultures. Using iGluSnFR as reporter, we found consistent changes in fluorescent signal that scaled with the magnitude of the delivered electrical stimulus. The corresponding changes in amplitude were surprisingly similar (up to 5-fold increase) to those that were originally documented for this reporter by the Looger group

(Marvin et al. 2013), suggesting high sensitivity and dynamic range. We have tested the platform with different excitatory reporters that measure pre-synaptic calcium, glutamate release, and post-synaptic calcium. However, in many neurodevelopmental disorders, an imbalance of excitatory and inhibitory synapses leads to circuit dysfunction, thus calling for functional markers of distinct synaptic subpopulations. Our platform should be perfectly set for measuring any of these reporters as long as they display measurable fluctuations in fluorescence intensity. As yet, there are few such reporters available, but the field is rapidly gaining traction. To highlight a few, iGABASnFR was developed to report on gamma aminobutyric acid (GABA) binding (Marvin et al. 2019), cholinergic synapses can be monitored using iAChSnFR (Borden et al. 2020) and dopaminergic synapses using $GRAB_{DA}$ (Sun et al. 2018). Such markers could readily be implemented in our platform. Similarly, with minor changes, it may be used for assessing changes in spontaneous (and evoked) activity in human patient-derived neurons.

While conceived for the analysis of population-level changes in synapse activity, the single synapse resolution allows revealing the stochasticity and probabilistic nature of synaptic transmission as exemplified by examples of occasional synaptic failures (Suppl. Fig. S2). We have not specifically elaborated on this topic here, but it is conceivable that this type of spatiotemporally resolved information can be exploited for quantal analysis, as presented by others (Farsi et al. 2021; James et al. 2019), but now in high-throughput format.

The in-depth analysis of extracted synapse activity parameters as we have now developed it, allows discriminating compounds by their modus operandi. To illustrate this, we created a small similarity matrix from which a recommender system for retrieving similar compounds can be built (Simm et al. 2018). From this pilot experiment, we were able to find correlations between the working mechanism of TBOA and WAY that are known to block clearance of

neurotransmitter by blocking glutamate transporters and differentiate it from the working mechanism of PMA which is a Protein Kinase C activator known to enhance neurotransmitter release. Per compound all extracted features were evaluated and ranked as a function of the quality by which they characterize the mode of action of a particular compound. Based on these features, other machine learning algorithms such as support vector machine networks or deep neural networks (Cortes and Vapnik 1995; Kotsiantis et al. 2006) can be used to classify and predict modes of action.

Conclusion

We have developed a fully integrated pipeline to analyze synapse activity with high throughput and content. The associated open-source software allows image processing, and metadata warehousing as well as downstream data analysis and visualization. Owing to its modular build, the software allows hierarchical data structuring and analysis. We believe this new platform, will represent a useful tool for profiling genetic and pharmacological perturbations aimed at improving synaptic performance in large scale screens.

Data Availability

The S3T software has been made publicly available on GitHub (https://www.github.com/S3Toolbox). The datasets generated during and/or analysed during the current study are available from the corresponding author on reasonable request.

Acknowledgements

This work was supported by VLAIO (grant # HBC.2019.2926). We thank Manu Sneyders from Peira BVBA for the fabrication of the stimulation device and sharing of its technical information. Dries Crauwels is acknowledged for developing the Labview tool.

Conflicts of Interest

HL, JPA are full-time employees of Janssen Pharmaceutica

Author Contributions

MVD – conceived, designed, and validated S3T, analyzed data, wrote the manuscript

RM – performed experiments and analyzed data, critically read and approved the manuscript

FP – performed experiments and analyzed data, critically read and approved the manuscript

PV – performed experiments, critically read and approved the manuscript

JPA – provided pharmacological expertise, critically read and approved the manuscript

HL – conceived the project, critically read and approved the manuscript

NDK – conceived the project, wrote the grant, built the instrumentation, designed molecular biology constructs, designed the experiments, supervised the project

WDV –wrote the grant, designed the experiments, supervised the project, wrote the manuscript

References

Borden, P. M., Zhang, P., Shivange, A. V., Marvin, J. S., Cichon, J., Dan, C., et al. (2020). A fast genetically encoded fluorescent sensor for faithful in vivo acetylcholine detection in mice, fish, worms and flies. *bioRxiv*, 2020.02.07.939504. https://doi.org/10.1101/2020.02.07.939504

Christiansen, E. M., Yang, S. J., Ando, D. M., Javaherian, A., Skibinski, G., Lipnick, S., et al. (2018). In Silico Labeling: Predicting Fluorescent Labels in Unlabeled Images. *Cell*, *173*(3), 792-803.e19. https://doi.org/10.1016/j.cell.2018.03.040

Chu, Y., Jin, X., Parada, I., Pesic, A., Stevens, B., Barres, B., & Prince, D. A. (2010). Enhanced synaptic connectivity and epilepsy in C1q knockout mice. *Proceedings of the National Academy of Sciences*, *107*(17), 7975–7980. https://doi.org/10.1073/pnas.0913449107

Cortes, C., & Vapnik, V. (1995). Support-vector networks. *Machine Learning*, *20*(3), 273–297. https://doi.org/10.1007/bf00994018

Dreosti, E., Odermatt, B., Dorostkar, M. M., & Lagnado, L. (2009). A genetically encoded reporter of synaptic activity in vivo. *Nature Methods*, *6*(12), 883–889. https://doi.org/10.1038/nmeth.1399

Eckart, C., & Young, G. (1936). The approximation of one matrix by another of lower rank. *Psychometrika*, *1*(3), 211–218. https://doi.org/10.1007/bf02288367

Farsi, Z., Walde, M., Klementowicz, A. E., Paraskevopoulou, F., & Woehler, A. (2021). Single synapse glutamate imaging reveals multiple levels of release mode regulation in mammalian synapses. *iScience*, *24*(1), 101909. https://doi.org/10.1016/j.isci.2020.101909

Hempel, C. M., Sivula, M., Levenson, J. M., Rose, D. M., Li, B., Sirianni, A. C., et al. (2011). A System for Performing High Throughput Assays of Synaptic Function. *PLoS ONE*, *6*(10), e25999. https://doi.org/10.1371/journal.pone.0025999

James, B., Darnet, L., Moya-Díaz, J., Seibel, S.-H., & Lagnado, L. (2019). An amplitude code transmits information at a visual synapse. *Nature Neuroscience*, *22*(7), 1140–1147. https://doi.org/10.1038/s41593-019-0403-6

Johnson, G. R., Donovan-Maiye, R. M., & Maleckar, M. M. (2017). Generative Modeling with Conditional Autoencoders: Building an Integrated Cell. *arXiv*.

Kotsiantis, S. B., Zaharakis, I. D., & Pintelas, P. E. (2006). Machine learning: a review of classification and combining techniques. *Artificial Intelligence Review*, *26*(3), 159–190. https://doi.org/10.1007/s10462-007-9052-3

Lathauwer, L. D., Moor, B. D., & Vandewalle, J. (2000). A Multilinear Singular Value Decomposition. *SIAM Journal on Matrix Analysis and Applications*, *21*(4), 1253–1278. https://doi.org/10.1137/s0895479896305696

Lin, M. Z., & Schnitzer, M. J. (2016). Genetically encoded indicators of neuronal activity. *Nature neuroscience*, *19*(9), 1142–1153. https://doi.org/10.1038/nn.4359

Lu, B., Nagappan, G., Guan, X., Nathan, P. J., & Wren, P. (2013). BDNF-based synaptic repair as a disease-modifying strategy for neurodegenerative diseases. *Nature Reviews Neuroscience*, *14*(6), 401–416. https://doi.org/10.1038/nrn3505

Mao, T., O'Connor, D. H., Scheuss, V., Nakai, J., & Svoboda, K. (2008). Characterization and Subcellular Targeting of GCaMP-Type Genetically-Encoded Calcium Indicators. *PLoS ONE*, *3*(3), e1796. https://doi.org/10.1371/journal.pone.0001796.g007

Marvin, J. S., Borghuis, B. G., Tian, L., Cichon, J., Harnett, M. T., Akerboom, J., et al. (2013). An optimized fluorescent probe for visualizing glutamate neurotransmission. *Nature Methods*, *10*(2), 162–170. https://doi.org/10.1038/nmeth.2333

Marvin, J. S., Shimoda, Y., Magloire, V., Leite, M., Kawashima, T., Jensen, T. P., et al. (2019). A genetically encoded fluorescent sensor for in vivo imaging of GABA. *Nature Methods*, *16*(8), 763–770. https://doi.org/10.1038/s41592-019-0471-2

Nieland, T. J. F., Logan, D. J., Saulnier, J., Lam, D., Johnson, C., Root, D. E., et al. (2014). High content image analysis identifies novel regulators of synaptogenesis in a high-throughput RNAi screen of primary neurons. *PLoS ONE*, *9*(3), e91744. https://doi.org/10.1371/journal.pone.0091744

Otsu, N. (1979). A Threshold Selection Method from Gray-Level Histograms. *IEEE Transactions on Systems, Man, and Cybernetics*, *9*(1), 62–66. https://doi.org/10.1109/tsmc.1979.4310076

Pnevmatikakis, E. A., Soudry, D., Gao, Y., Machado, T. A., Merel, J., Pfau, D., et al. (2016). Simultaneous Denoising, Deconvolution, and Demixing of Calcium Imaging Data. *Neuron*, *89*(2), 285–299. https://doi.org/10.1016/j.neuron.2015.11.037

Simm, J., Klambauer, G., Arany, A., Steijaert, M., Wegner, J. K., Gustin, E., et al. (2018). Repurposing High-Throughput Image Assays Enables Biological Activity Prediction for Drug Discovery. *Cell Chemical Biology*, *25*(5), 611-618.e3. https://doi.org/10.1016/j.chembiol.2018.01.015

Sun, F., Zeng, J., Jing, M., Zhou, J., Feng, J., Owen, S. F., et al. (2018). A Genetically Encoded Fluorescent Sensor Enables Rapid and Specific Detection of Dopamine in Flies, Fish, and Mice. *Cell*, *174*(2), 481-496.e19. https://doi.org/10.1016/j.cell.2018.06.042

Tampellini, D. (2015). Synaptic activity and Alzheimer's disease: a critical update. *Frontiers in Neuroscience*, *9*, 423. https://doi.org/10.3389/fnins.2015.00423

Verschuuren, M., Verstraelen, P., Barriga, G. G.-D., Cilissen, I., Coninx, E., Verslegers, M., et al. (2019). High-throughput microscopy exposes a pharmacological window in which dual leucine zipper kinase inhibition preserves neuronal network connectivity. *Acta Neuropathologica Communications*, *7*(1), 6. https://doi.org/10.1186/s40478-019-0741-3

Verstraelen, P., Barriga, G. G.-D., Verschuuren, M., Asselbergh, B., Nuydens, R., Larsen, P. H., et al. (2020). Systematic Quantification of Synapses in Primary Neuronal Culture. *iScience*, *23*(9), 101542. https://doi.org/10.1016/j.isci.2020.101542

Virdee, J. K., Saro, G., Fouillet, A., Findlay, J., Ferreira, F., Eversden, S., et al. (2017). A high-throughput model for investigating neuronal function and synaptic transmission in cultured neuronal networks. *Scientific Reports*, *7*(1), 127. https://doi.org/10.1038/s41598-017-15171-5

Wardill, T. J., Chen, T.-W., Schreiter, E. R., Hasseman, J. P., Tsegaye, G., Fosque, B. F., et al. (2013). A neuron-based screening platform for optimizing genetically-encoded calcium indicators. *PLoS ONE*, *8*(10), e77728. https://doi.org/10.1371/journal.pone.0077728

Zoghbi, H. Y., & Bear, M. F. (2012). Synaptic dysfunction in neurodevelopmental disorders associated with autism and intellectual disabilities. *Cold Spring Harbor Perspectives in Biology*, *4*(3). https://doi.org/10.1101/cshperspect.a009886

Figures

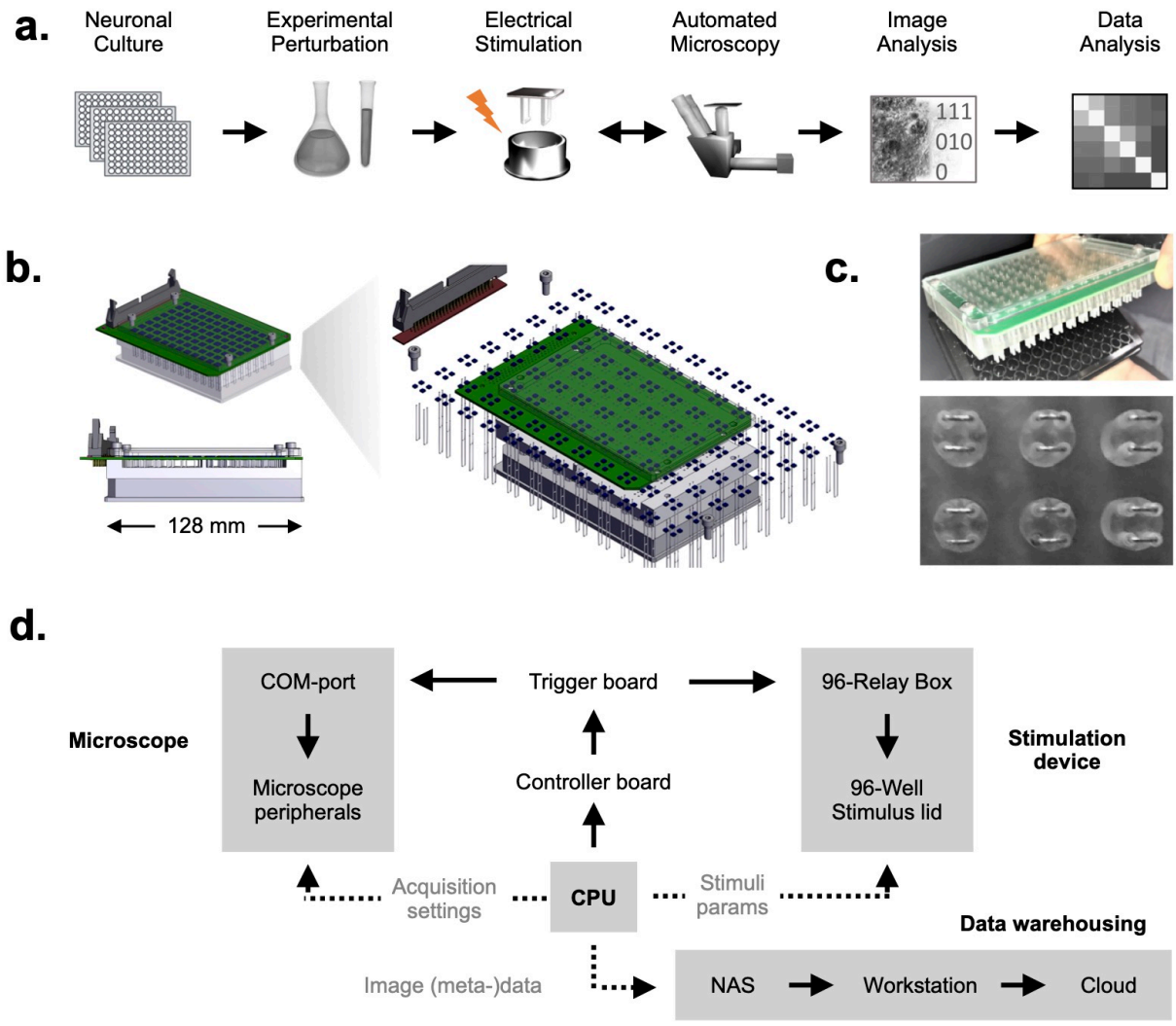

Figure 1. A high-throughput pipeline for measuring electrically evoked synaptic activity. a) General summary of the major elements of the pipeline; b) 3D model views of the stimulation device (top, side, and exploded view); c) 96-well plate with stimulation device as top lid (top) and bottom view of part of the stimulation device showing the individual platinum electrodes (bottom); d) Schematic summary of the hardware and software integration.

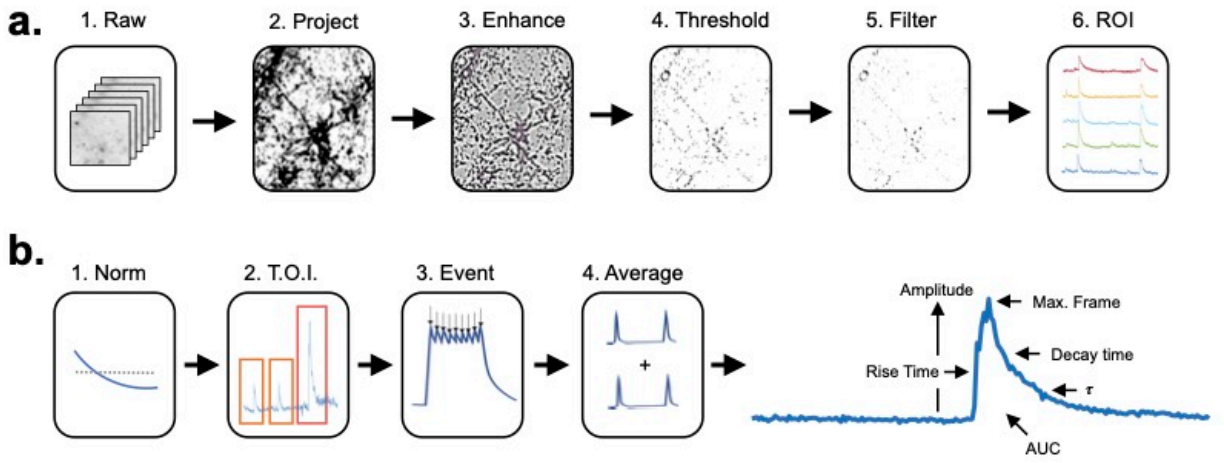

Figure 2. S³T software pipeline. a) The stack of raw images serves as input (1) and is projected (e.g., using SVD) (2), resulting in a high SNR image. In this image, spatial features can be further enhanced by spatial filters (e.g., Laplacian) (3) after which an automatic threshold is set, resulting in a binary image (4), onto which morphological filtering is done (5). This results in a mask, which is applied onto the original image to extract responses of individual regions of interest (ROIs) (6); b) For the analysis of the synapse responses, the absolute intensity of the pixels is calibrated based on the intensity of the darkest pixels (1). For each ROI, one or more time-window of interest (TOI) is extracted based on the stimulation timings (2). In each window, different events are detected (3). Similar stimulation responses are averaged over time and over different ROIs (4). The subsequent analysis of each event consists of the extraction of different features (Suppl. Data 4) of which several are illustrated.

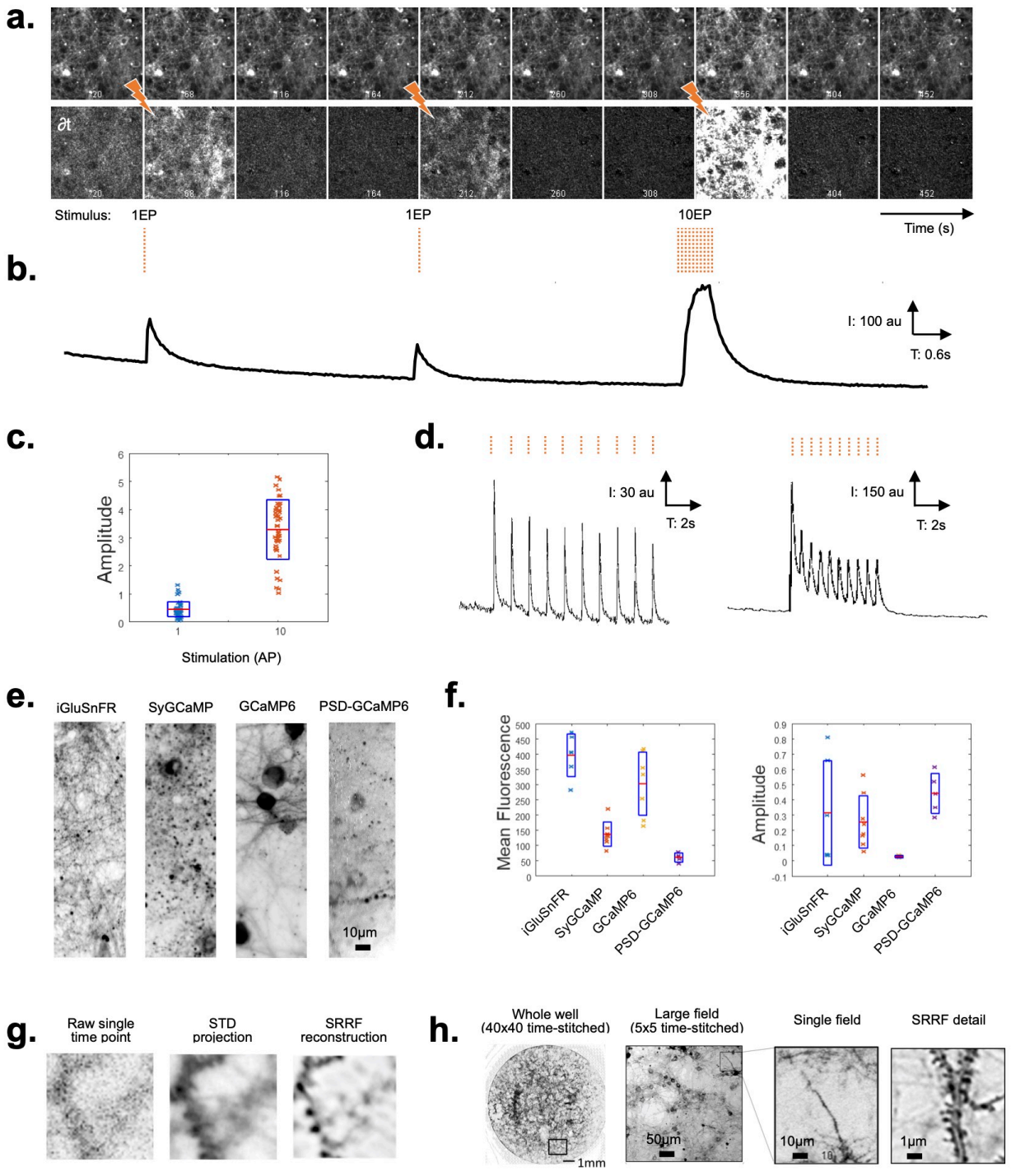

Figure 3. High-throughput imaging allows assessment of electrically evoked synapse activity at multiple scales. a) Montage of selected frames from electrically stimulated primary hippocampal neurons expressing iGluSnFR (top) and their difference with the average frame

(bottom); b) corresponding intensity profile of the image; c) Response amplitude (mean ± stdev) to 1EP and 10 EP stimulation for different wells (field average); d) Responses to electric stimulation patterns with different pulse intervals; e) Temporally averaged intensity projection (time-stack average) of recordings with different markers, inverted for clarity; f) Mean fluorescence and amplitude of different fluorescent markers; g) Comparison of image quality in a single raw image versus that of a standard deviation (STD)-projected or SRRF reconstructed version of a time-lapse acquisition of iGluSnFR-transduced neurons; h) Multi-scale acquisitions of iGluSNFR-transduced neurons, as obtained from stitching sequential acquisitions up to a whole well and down to a single spine by SRRF reconstruction.

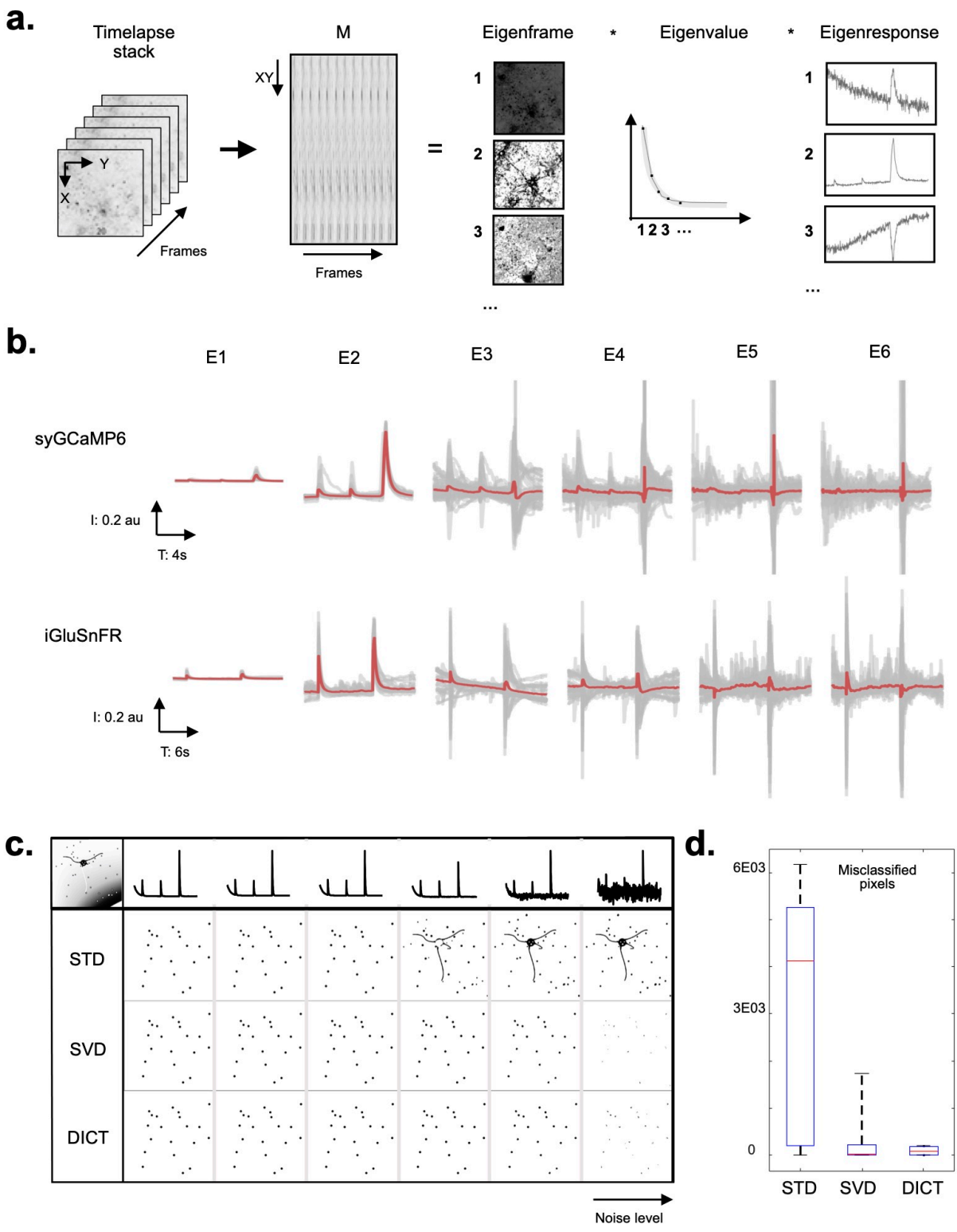

Figure 4. SVD is a robust approach for synapse analysis. a) Visual representation of converting the image stack into a matrix for singular value decomposition from which left eigenvectors

represent eigenframes, and the right eigenvectors represent the eigenresponses; b) The first 6 eigenresponses (E1-E6) for a representative dataset of responding syGCaMP6f (n = 42 wells, two stimuli) and iGluSnFR (n = 32 wells, three stimuli) expressing cells. E2 contains the most prominent and consistent response, whereas higher-order eigenresponses progressively become more variable and contain more noise. Individual traces are depicted in gray and the average response in red; c) Illustration of mask creation on artificially created sample data with STD, SVD, and DICT for increasing amounts of noise. d) A bar plot indicating the total number of errors made for each method over a benchmark of 60 different movies with different amounts of simulated noise and photobleaching

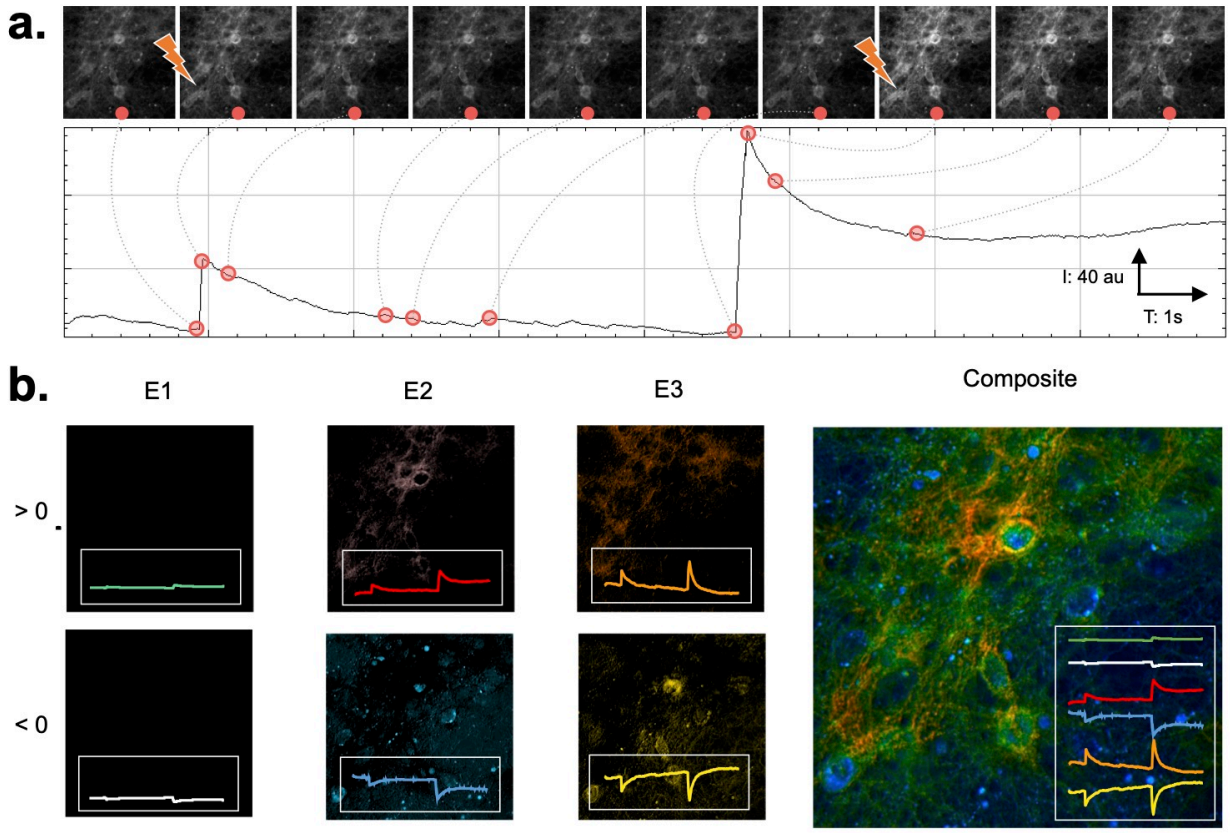

Figure 5. SVD allows spatiotemporal unmixing of synapse activity. a) Selected frames and field-average intensity response curve from a 1EP + 10EP stimulation recording on iGluSnFR-expressing neurons; b) Color-coded representation of the positive and negative part of the first three eigen-components (eigenframe and eigenresponse) of SVD reveal the dynamics in the field of view. Line profiles represent the resp. contribution of the eigenframes to the temporal signal.

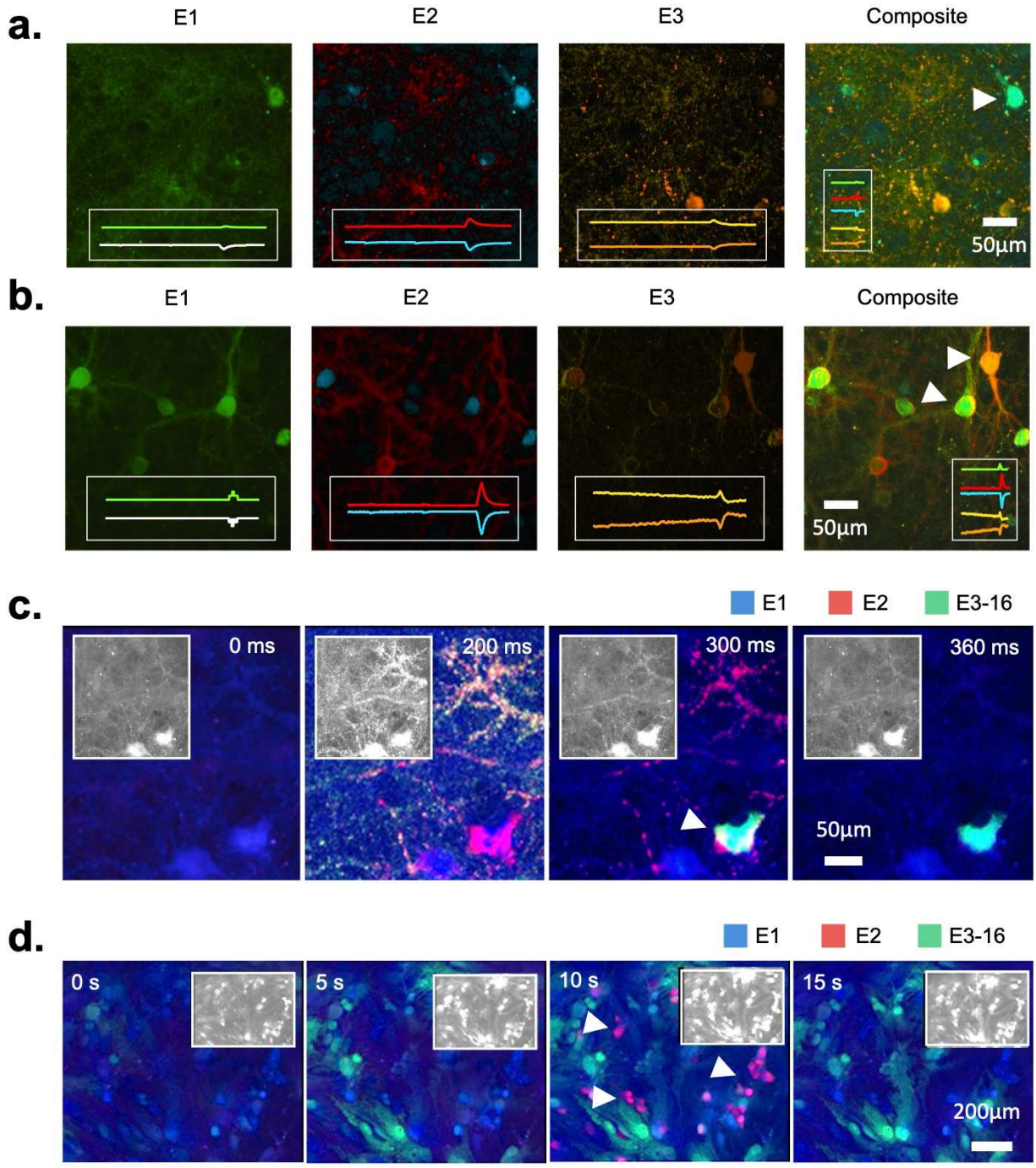

Figure 6. SVD allows spatiotemporal unmixing of cell types. a) Spatiotemporal deconvolution using the first 3 eigenframes on a SyGCaMP6f recording, reveals differential dynamics of somatic (arrowhead) and synaptic regions; b) Applied to a GCaMP6f recording, SVD

deconvolution discriminates responding from non-responding cells (arrowheads); c) More inclusive SVD deconvolution reveals differential dynamics of synapses and astrocyte body (arrowhead) in a PSD95-GCaMP6f recording. Inset shows the original grayscale image; d) The same extended SVD deconvolution allows differentiating neuronal (arrowheads) from astrocyte dynamics in Fluo-4AM labeled cultures, stimulated with glutamate. Inset represents the original grayscale image.

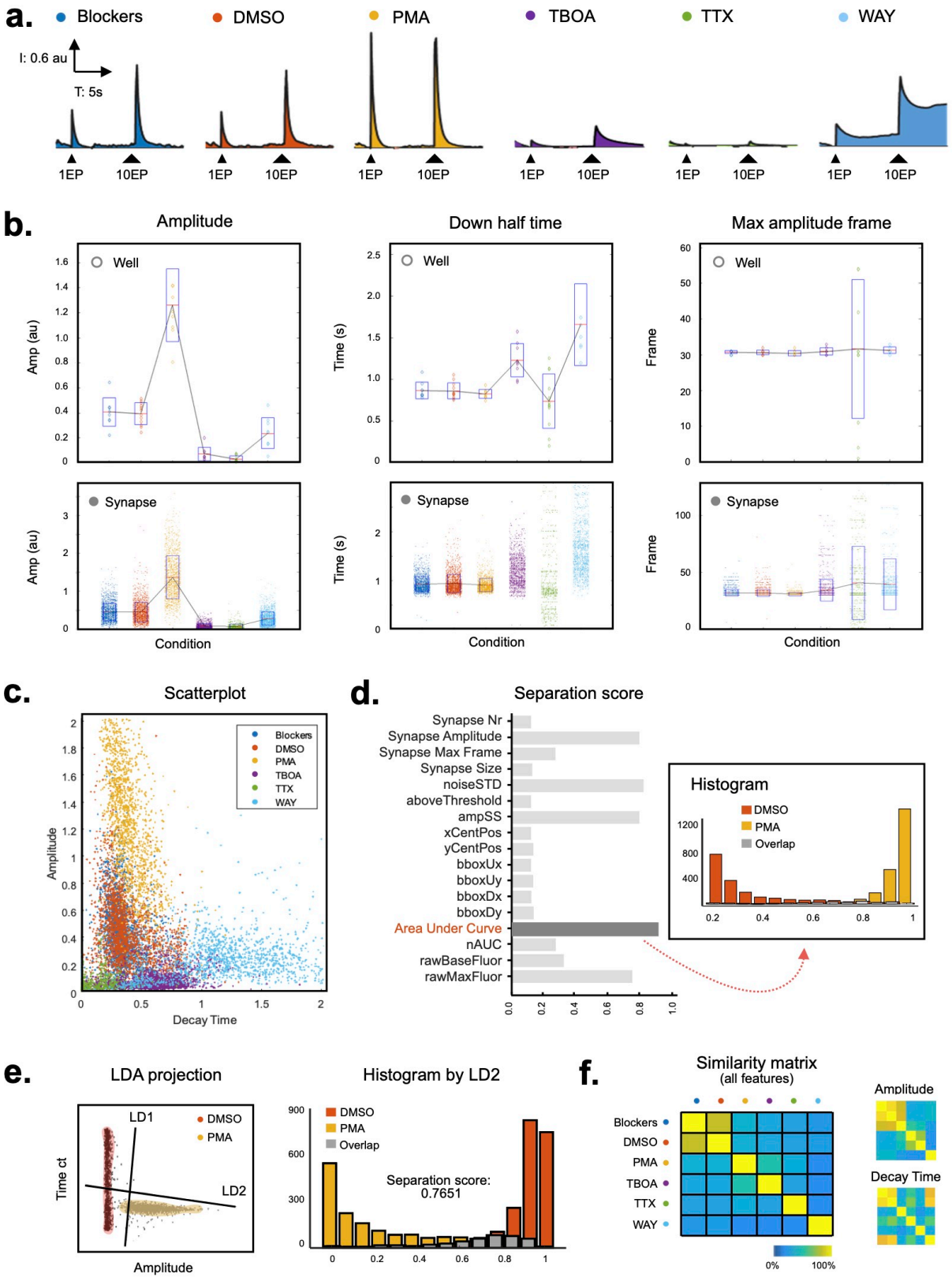
a.
Blockers
DMSO
PMA
TBOA
TTX
WAY
I: 0.6 au
T: 5s
1EP
10EP
b.
Amplitude
Down half time
Max amplitude frame
Well
Synapse
Amp (au)
Time (s)
Frame
Condition
c.
Scatterplot
Amplitude
Decay Time
d.
Separation score
Synapse Nr
Synapse Amplitude
Synapse Max Frame
Synapse Size
noiseSTD
aboveThreshold
ampSS
xCentPos
yCentPos
bboxUx
bboxUy
bboxDx
bboxDy
Area Under Curve
nAUC
rawBaseFluor
rawMaxFluor
Histogram
DMSO
PMA
Overlap
e.
LDA projection
Histogram by LD2
LD1
LD2
Time ct
Amplitude
Separation score:
0.7651
f.
Similarity matrix
(all features)
Amplitude
Decay Time
0%
100%

Figure 7. Integrated synapse analysis for compound screening and classification on iGluSnFR-expressing neurons. a) average traces of synapse responses in cortical neuronal cultures treated with one six compounds (or control) and sequentially stimulated with 1EP and 10EP; b) Compound data visualization of parameters amplitude, down half time and max frame at the level of the well and at the level of the individual synapse; c) Scatterplot of two discriminating synapse response parameters (amplitude and decay time); d) Separation scores between treatment with DMSO or PMA as determined for different parameters and illustration of the corresponding histogram for synapse response AUC; e) LDA of all parameters for the comparison PMA vs DMSO reveals that amplitude is a dominant contributor as also revealed by the histogram of the corresponding projection onto LD2; f) Similarity score for each combination of compounds when separated by LDA using all features, or when using only amplitude or decay (small insets).